



## DROPLET-WALL COLLISIONS: EXPERIMENTAL STUDIES OF THE DEFORMATION AND BREAKUP PROCESS

CHR. MUNDO, M. SOMMERFELD and C. TROPEA

Lehrstuhl für Strömungsmechanik, Universität Erlangen-Nürnberg, Cauerstr. 4,  
91058 Erlangen, Germany

(Received 3 April 1994; in revised form 1 October 1994)

**Abstract**—Experimental studies of liquid spray droplets impinging on a flat surface have been performed with the aim of formulating an empirical model describing the deposition and the splashing process. Monodisperse droplets with a known viscosity and surface tension, produced by a vibrating orifice generator, were directed towards a rotating disc and the impingement was visualized using an illumination synchronized with the droplet frequency. A rubber lip was used on the rotating disk to remove any film from previous depositions.

The test matrix involved different initial droplet diameters ( $60 < d_0 < 150 \mu\text{m}$ ), velocities ( $12 < w < 18 \text{ m/s}$ ), impingement angles ( $4^\circ < \alpha < 65^\circ$ ), viscosities ( $1.0 < \mu < 2.9 \text{ mPas}$ ) and surface tensions ( $22 < \sigma < 72 \text{ mN/m}$ ). The liquids used to establish the different viscosities and surface tensions were ethanol, water and a mixture of water-sucrose-ethanol.

One major result from the visualization is a correlation of the deposition-splashing boundary in terms of Reynolds number and Ohnesorge number. Noteworthy is that a distinct correlation between the Re and Oh number,  $K = \text{Oh} \cdot \text{Re}^{1.25}$ , is only achieved if the normal velocity component of the impinging droplets is used in these dimensionless numbers.

For the case of a splashing droplet, a two-component phase Doppler anemometer was used to characterize the size and velocity of the secondary droplets. The obtained droplet size distributions and correlations between droplet size and velocity around the point of impingement constitute the basis of an empirical numerical model.

*Key Words:* spray systems, droplet-wall interaction, impact models

### 1. INTRODUCTION

The fluid mechanics of spray droplets impinging on a rigid surface is of great importance in many different technical applications, including thin film coatings, spray painting, spray coating, injection systems and in the spraying of molten metal for the production of semi-finished articles with a special metallurgical structure. Although numerous studies have been performed in the past on droplet-wall interactions, most of these are qualitative in nature, obtaining information from the visualization of droplet impingement and deformation. A short summary of previous studies is given in the following section.

In general there are two possible outcomes of droplet impingement on a solid and dry surface, each of which may be desirable for a particular application. On the one hand the droplet may deposit on the surface and form a liquid film. For more energetic impacts however, the droplet splashes and secondary droplets are formed. Some general correlations exist describing this deposition-splashing limit and its governing parameters, however virtually no information exists describing the size and velocity distributions of the secondary droplets and the splashed mass fraction with reference to the impingement parameters. This information is, however, essential if droplet-wall interactions are to be modelled with the intent of incorporating such models into an Eulerian-Lagrangian approach for calculating two-phase flows.

The goal of the present investigation is to provide such information in a form suitable to formulate empirical models of the droplet-wall interaction. For this purpose the secondary droplets must be measured in size, concentration and velocity. Therefore, a phase Doppler anemometer (PDA) has been employed, in addition to more traditional visualization techniques.

Following a brief literature review of previous experimental studies, some theoretical considerations of the droplet-wall interaction are given in section 2. In particular, dimensionless analysis

can help to identify important governing parameters and also guide the layout of the experimental equipment and procedures. Details of the experimental equipment are given in section 3 before presenting the measurement results in section 4. A summary of the most important conclusions is given in section 5.

### 1.1. Previous investigations of droplet impact on surfaces

The outcome of a droplet impact on a solid surface depends on the properties of the liquid, the surface conditions and the kinematic parameters, i.e. velocity and momentum. Following the Buckingham II-theorem, the number of independent parameters can be reduced by the number of fundamental dimensions which are present. Usually the remaining number of parameters which are important for a particular experiment is, however, relatively large. Therefore, it is often difficult to obtain simple relations from dimensional analysis and results reported in previous investigations are often not comparable to one another.

Nevertheless, the major dimensionless groups governing droplet impact include

$$\text{Reynolds number } \text{Re} = \frac{\rho d_0 w_0}{\mu} \quad [1]$$

$$\text{Ohnesorge number } \text{Oh} = \frac{\mu}{\sqrt{\rho \sigma d_0}} \quad [2]$$

$$\text{and surface roughness } S_t = \frac{R_t}{d_0} \quad [3]$$

where  $\rho$ ,  $\mu$  and  $\sigma$  are the liquid density, the viscosity and the surface tension for a fluid–air interface. Furthermore,  $d_0$  is the initial droplet diameter and  $R_t$  the mean roughness height of the wall surface. Note that the droplet initial velocity  $w_0$  used in the Reynolds number is the component normal to the surface.

The Weber number is also commonly used

$$\text{We} = (\text{Oh} \cdot \text{Re})^2 = \frac{\rho d_0 w_0^2}{\sigma} \quad [4]$$

as well as the Bond number

$$\text{Bo} = \frac{d_0^2 \rho g}{\sigma} \quad [5]$$

where  $g$  is the gravitational force, in cases in which a film on the surface may have an influence on the impact event.

Previous investigations which have been performed on droplet impingement on surfaces may conveniently be divided into three main groups (Rein 1992):

- Investigations of droplet impingement on heated surfaces, in which the temperature is above the evaporation temperature of the fluid.
- Investigations of droplet impingement on cold surfaces.
- Investigations of droplet impingement on films.

*1.1.1. Impact on heated surfaces.* Obviously the most important technical application in this area is the spray cooling of hot surfaces and the impingement of injected fuel droplets onto the heated surfaces of a combustion engine.

The early work by Wachters & Westerling (1963) considered the heat transfer of single droplets impinging on a heated surface. They determined the heat flux and evaporation rate for surface temperatures above the evaporation temperature. Furthermore, they found that, for low Weber numbers of the impinging droplet, the droplet could experience a reflection from the surface, as indicated in figure 1. This can be explained by the vapour layer, which is generated due to the sudden evaporation of the liquid immediately above the solid surface, and which expels the droplet from the surface. These observations were supported by the investigations of Anders *et al.* (1993) who observed a reflection of a sequence of 90  $\mu\text{m}$  droplets on a heated surface for a small velocity

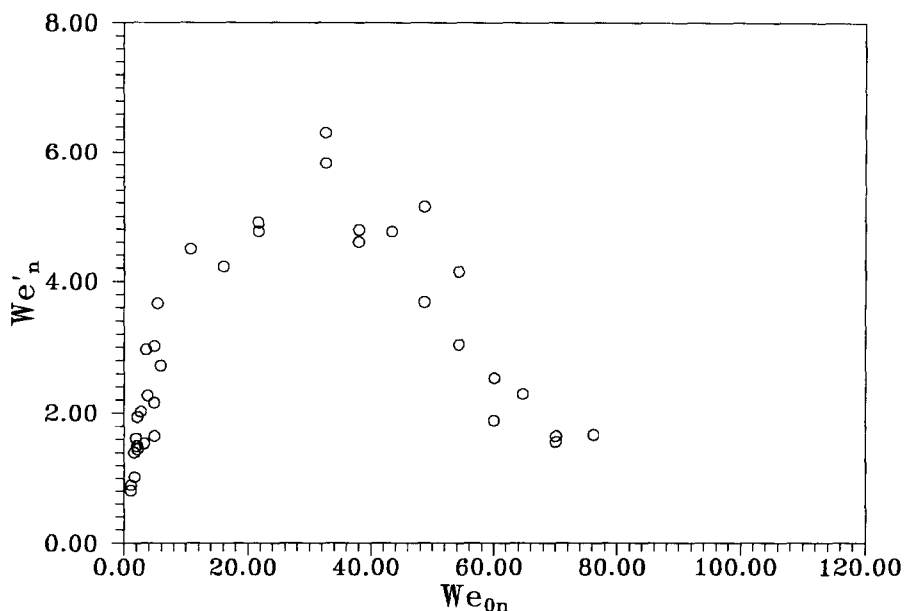


Figure 1. Relationship between the normal velocity components at arrival and departure for a droplet impinging on a heated plate (Wachters & Westerling 1963).

component normal to the wall. For higher Weber numbers the droplet was deformed and the reflection velocity vector decreased. For Weber numbers above a critical value, the droplets splashed into secondary droplets. Bolle & Moureau (1982) extended these investigations to polydisperse spray-wall interaction.

Chandra & Avedisian (1991) employed photographic measuring techniques to evaluate the deformation stages of a single droplet impinging on both heated and unheated surfaces at low Reynolds numbers.

*1.1.2. Impact on unheated surfaces.* Levin & Hobbs (1971) used a copper hemisphere on which water droplets of about 2.9 mm in diameter impinged at a low velocity normal to the surface. If the kinetic energy of the primary droplets was high enough, then the droplets were deformed to a cylindrical sheet that rose around the point of impingement. Often this sheet was unstable and tiny droplets appeared at its upper rim. This occurrence was called *corona formation*. For evaluating the diameter distribution of the splashed droplets only those droplets greater than 50  $\mu\text{m}$  in size could be counted, due to the insufficient resolution of the photographs. The number averaged diameter was between 10 and 20% of the primary droplet diameter. When the kinetic energy was relatively low, the droplets were deformed during the impact but splashing did not occur. In this case, the fluid was completely deposited on the surface.

Stow & Hadfield (1981) tried to evaluate the size distribution of splashed droplets more precisely than Levin & Hobbs (1971). They used photographic emulsion paper on which the splashed droplets were collected, increasing the resolution to droplets smaller than 50  $\mu\text{m}$ . They found that the splash-product sizes were distributed according to a log-normal distribution function and that the number averaged diameter was about 10% of the primary droplet diameter. Comparing the results for different impingement conditions, one finds that an increase of the surface tension led to an increase of the size of the generated droplets, and that an increase of the diameter of the primary droplets also led to an increase of the size of the splashed droplets. Weiss (1993) found similar relations for droplets impinging on a surface film with a high repetition frequency. Walzel (1980) analysed the splashing of water-glycerin mixtures on dry and wetted surfaces. Using the Buckingham II-theorem he obtained a set of two non-dimensional parameters which determine whether splashing or deposition took place. The non-dimensional parameters include fluid properties (surface tension, viscosity and density) and kinematic parameters (velocity normal to the wall and diameter).

$$d_0^* = \frac{d_0 \rho \sigma}{\mu^2} \quad [6]$$

$$\sqrt{\frac{We}{d_0^*}} = \frac{w_0 \mu}{\sigma} \quad [7]$$

Schmidt & Knauss (1976) investigated the splashing of mercury droplets in a rotary atomizer. The background of these experiments was the atomization of molten metal which is used for metal products with a special metallurgical structure. In section 4.2 it will be shown that the data of Schmidt & Knauss (1976) agree well with the correlations found in the present study.

In recent years the development of laser-diffraction and laser-Doppler measuring techniques have provided an opportunity to measure both the velocity and the size of spray droplets. Hardalupas *et al.* (1991) measured the droplet size and velocity distribution of a fuel spray near the surface of a disc. In their experiments they showed that the size distribution of splashed droplets depended on the inclination angle of the primary spray.

Brunello *et al.* (1991) investigated the impingement of a spray for a defined inclination angle with respect to the surface using a phase-Doppler anemometer. They found a bimodal diameter distribution in the vicinity of the wall, indicating that a second size fraction was generated by the impact.

Summarizing the studies on droplet-wall interactions performed by various investigators, one can conclude that an attempt was made to characterize the outcome of the splashing. However, the influencing parameters were not varied in a wide range to obtain an empirical model or a numerical model that could be implemented into a two-phase flow simulation code.

*1.1.3. Impact on fluid films.* The investigations of Jayaratne & Mason (1964) show that for very low impingement momentum (and therefore low Weber number normal to the wall), water droplets can rebound from a water surface. Özdemir & Whitelaw (1992) investigated the spray impingement on an unheated surface covered by a fluid film and found that the impact on the wall generates a new fraction of larger droplets which are spattered out of the liquid film.

## 2. THEORETICAL APPROACH

### 2.1. Deformation process

A full description of the fluid motion during the impact and the deformation process can, in principle, be obtained solving the Navier–Stokes equations, and a number of authors have numerically studied the deformation of an impinging droplet on this basis. Foote (1974) solved the equations with the Marker-and-Cell-method (MAC) and obtained a solution for low *Re* and *We* numbers for the impinging primary droplet. Van der Geld & Sluyter (1987) used the collocation method to determine the motion of discrete surface points of a droplet that rests on a surface with  $w_0 = 0$ . For the case of higher *Re* and *Oh* numbers, with a deformation that leads to a corona and subsequent breakup, the droplet–wall collision has not been simulated.

### 2.2. Deposition–splashing of the droplet

Another important—and maybe easier—problem to solve is the quantification when breakup or complete deposition occurs. In principle the equations of energy conservation

$$\underbrace{E_k + E_p + E_s}_{\text{before impact}} = \underbrace{E'_k + E'_p + E'_s + E'_d}_{\text{after impact}} \quad [8]$$

and mass conservation

$$m = m' \quad [9]$$

have to be solved. Here,  $E_k$ ,  $E_p$ ,  $E_s$  and  $E_d$  are the kinetic, potential, surface and dissipated energies, and  $m$  and  $m'$  are the mass of the droplets before and after impact, respectively. For the case that

$E'_d \approx E_k + E_p + E_s$  splashing does not occur and complete deposition of the fluid mass takes place. The kinetic and surface energy before impact can be described by

$$E_k = \frac{1}{12} \rho_L w_0^2 \pi d_0^3 \quad [10]$$

$$E_s = \pi d_0^2 \sigma. \quad [11]$$

where  $\rho_L$ ,  $\sigma$ ,  $d_0$  are the liquid density, surface tension and diameter of the impacting droplet. The kinetic energy upon impact is expended in deforming the droplet and, for the case that a corona is not formed and full deposition takes place; it becomes zero at the maximum extension of the liquid on the surface. At the maximum extension diameter  $d_{\max}$ , the surface energy can be described as (Chandra & Avedisian 1991)

$$E'_s = \frac{\pi}{4} d_{\max}^2 \sigma (1 - \cos \Theta). \quad [12]$$

The contact angle  $\Theta$  is defined using the tangent line at the liquid–gas interface at the point where the meniscus begins, as sketched in figure 2.

The dissipated energy is very difficult to determine, because the velocity distribution inside the deforming droplet is not known. Chandra & Avedisian (1991) used a very simple model to determine  $E'_d$

$$E'_d = \int_0^{t_c} \int_V \Phi \, dV \, dt \approx \Phi V t_c. \quad [13]$$

The dissipation per unit mass of the fluid is given by

$$\Phi = \mu \left( \frac{\partial u_x}{\partial y} + \frac{\partial u_y}{\partial x} \right) \frac{\partial u_x}{\partial y} \approx \mu \left( \frac{w_0}{h} \right)^2 \quad [14]$$

where  $t_c$ , the time for deformation, is estimated by  $t_c \approx d_0/w_0$ . The volume of the fluid  $V$  when it is flattened out in the shape of a disc is

$$V \approx \frac{\pi}{4} d_{\max}^2 h \quad [15]$$

where  $h$  represents the height of the disc.

Combining [8]–[15], introducing the Re and We numbers with  $\beta_{\max} = d_{\max}/d_0$  and  $E_p = E'_p$  the following equation for the splashing–deposition boundary is obtained

$$\frac{3}{2} \frac{\text{We}}{\text{Re}} \beta_{\max}^4 + (1 - \cos \Theta) \beta_{\max}^2 - \left( \frac{1}{3} \text{We} + 4 \right) = 0. \quad [16]$$

Introducing the Ohnesorge number  $\text{Oh} = \sqrt{\text{We}/\text{Re}}$  yields

$$\text{Oh} = \sqrt{\frac{3(1 - \cos \Theta) \beta_{\max}^2 - 12}{\text{Re}^2 - 4.5 \beta_{\max}^4 \text{Re}}} \quad [17]$$

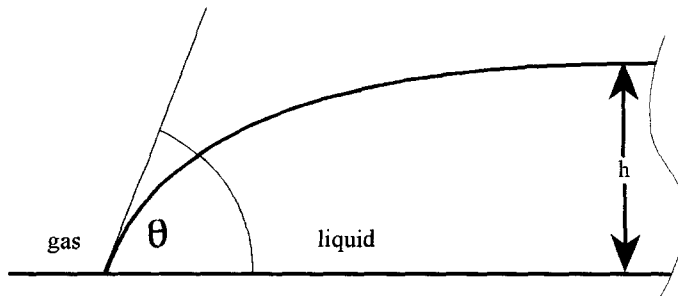


Figure 2. Definition of the contact angle  $\Theta$ .

Equation [17] determines the splashing–deposition boundary as a function of the Ohnesorge and the Reynolds numbers of the impinging droplet. For an Ohnesorge number above the value given in [17] splashing will occur, otherwise the fluid droplet will deposit completely on the surface. This equation confirms that the deposition–splashing depends only on the  $Re$  and  $Oh$  numbers, as expected from the dimensional analysis. The geometrical factor  $\beta_{\max}$  and the contact angle  $\Theta$  are constant for a given fluid and surface material. This theoretical approach will be compared to the measured splashing–deposition data presented in section 4.3.

### 3. EXPERIMENTAL SET-UP

In the present investigation, the impingement and deformation process of droplets on a rigid cold wall has been investigated by directing a stream of monodispersed droplets towards a rotating disc. The rotational speed of the disc determines the effective collision angle and the velocity of impingement. The normal component of the velocity remains independent of the disc rotational speed and is determined by the operating conditions of the droplet generator.

#### 3.1. Apparatus

A schematic diagram of the experimental set-up is shown in figure 3. The main components are:

- A droplet generator which produces a stream of monodisperse droplets in the size range of 60–150  $\mu\text{m}$  and a repetition rate of 28–65 kHz.
- A rotating disc with which the circumferential velocity can be varied in the range of 1.3–39.3 m/s.
- A rubber lip to remove the film of fluid that was deposited on the surface.

A vibrating orifice generator (TSI Model 3450) was used to generate a stream of monodisperse droplets (Berglund & Liu 1973). The droplets were formed by forcing liquid through an orifice of 50  $\mu\text{m}$  diameter. The outflowing jet was perturbed by a piezo quartz actuator acting on the orifice plate in the frequency range of 28–65 kHz, leading to perturbations of a defined wavelength and thus to a jet disintegration at a defined frequency and with a defined droplet volume.

The mean diameter  $d_0$  and mean velocity  $w_0$  of the monodispersed droplets after disintegration can be evaluated using [18] and [19]

$$d_0 = \sqrt[3]{\frac{6\dot{Q}}{\pi f}} \quad [18]$$

$$w_0 = v_{\text{syringe}} \frac{d_{\text{syringe}}}{d_{\text{orifice}}} \quad [19]$$

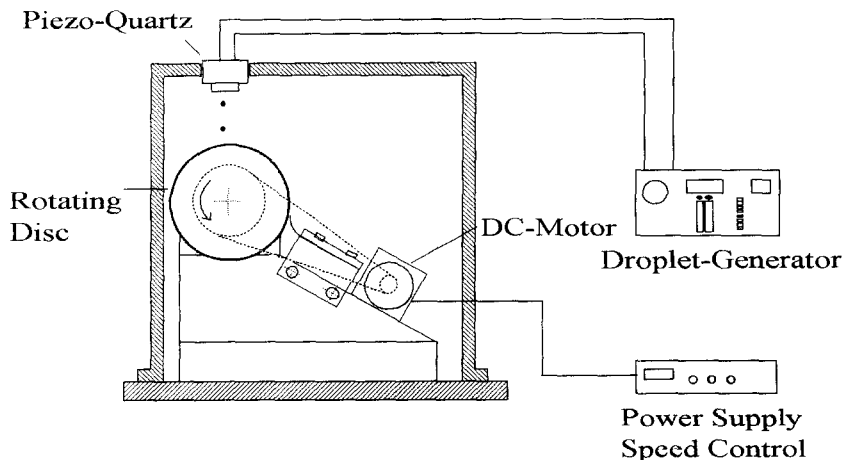


Figure 3. Schematic overview of the test rig.

where  $\dot{Q}$  is the total volume flow rate defined by the feed syringe velocity  $v_{\text{syringe}}$  and the diameter  $d_{\text{syringe}}$  and  $f$  is the piezo quartz actuator frequency.

This stream of droplets impinged on a rotating disc made of stainless steel. The co-ordinate system and the definition of the velocity components is shown in figure 4. The impact angle  $\alpha$  is defined as the angle between the absolute velocity vector and the normal on the surface. Therefore, the impingement occurred at a distinct impact angle and at a distinct impact velocity which was dependent on the rotational speed of the disc. The surface temperature of the disc was kept constant at 25°C.

Two different rotating discs were used during the experiments. Disc 1 had a technically smooth mean roughness height (i.e.  $R_t = 2.8 \mu\text{m}$ ) and disc 2 had a roughness height in the range of the impinging primary droplet diameter (i.e.  $R_t = 78 \mu\text{m}$ ). A non-dimensional roughness number can be defined as  $S_t = R_t/d_0$  (disc 1:  $S_t = 0.03$ ; disc 2:  $S_t = 0.86$ ). In figure 5 the surface profile of the two discs is shown. The experimental test conditions are summarized in table 1.

### 3.2. Instrumentation

**3.2.1. Visualization techniques.** For determining the boundary between droplet deposition and splashing a visualization technique was used. This visualization technique synchronizes an illuminating LED with the droplet impact. Therefore, each video frame represents an average over many single droplet impacts all at the same impact phase. Statistical fluctuations are eliminated or blurred on single frame pictures.

The instrumentation set-up is shown schematically in figure 6. The LED (Hewlett-Packard Type HLMP-8150 15 Candela) was triggered at the frequency of the droplet generator (28–65 kHz) with a pulse duration of 500 ns. Therefore, droplets of 100  $\mu\text{m}$  diameter and a velocity of 10 m/s could be measured with a spatial resolution of  $r_s = w_0 \Delta t/d_0 = 5\%$ . The maximum intensity of light of the LED was 423.5 mW/sr at a dominant wavelength of  $\lambda = 637 \text{ nm}$  (red light). The rise time of the LED-light pulse was determined as  $\Delta\tau = 45 \text{ ns}$ .

A CCD-camera (Type Hitachi KP-M1) with a high spatial resolution of  $756 \times 581$  pixels was used for acquiring the pictures. The camera was equipped with a 90 mm f4 macro lens and an extension bellows. The repetition rate for the CCD camera readout was 50 Hz, so that each frame consisted of 560–1300 events. Therefore, this measuring technique gave an *integral* view of the deformation process.

The pictures from the CCD-camera were recorded using a SVHS-videorecorder (Panasonic). From this videotape, pictures were taken with a Canon T90 camera (film: Kodak Tmax 400).

**3.2.2. Phase Doppler measurements.** For qualitatively analysing the outcome of a splashing collision a commercially available two-colour phase Doppler anemometer (PDA) was used. The technical data of the PDA are summarized in table 2 and in the user's manual (Dantec 1992). The PDA was aligned normal to the plane of impingement, so that the vertical and tangential velocity components of the impinging and reflected spray droplets could be measured.

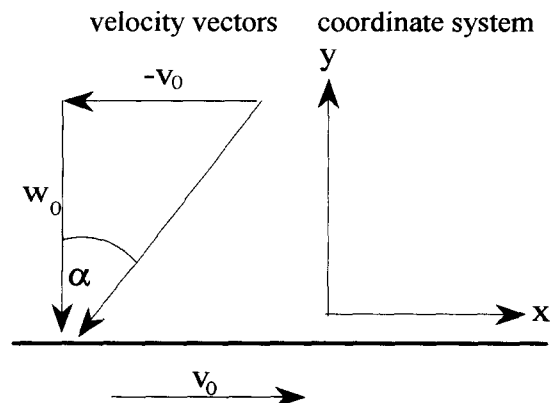
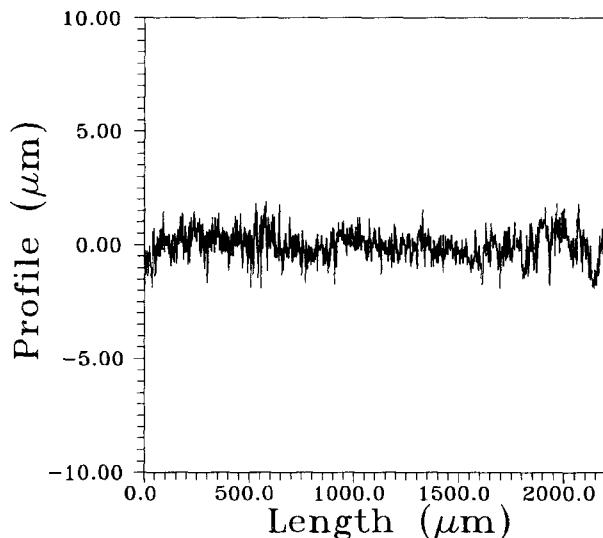


Figure 4. Co-ordinate system.

a)



b)

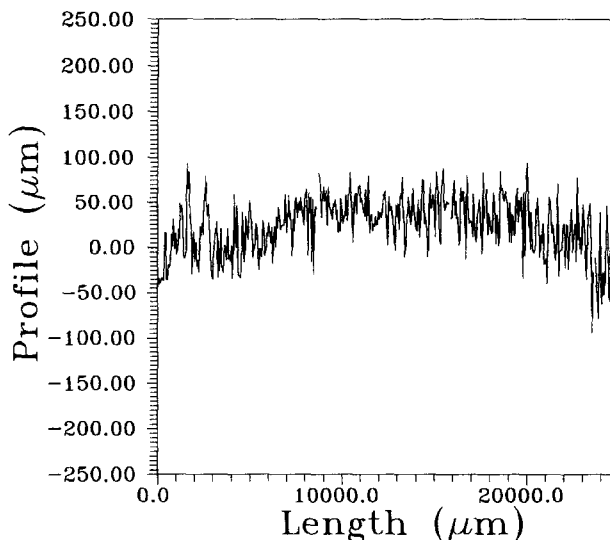


Figure 5. Surface profile of disc 1 (a) and disc 2 (b).

Table 1. Test conditions

Generated droplets		
Fluid	—	water-ethanol-sucrose
Viscosity	mPas	1-2.9
Surface tension	mN/m	22-72
Density	kg/m <sup>3</sup>	789-998
Diameter	μm	60-150
$w_{0,n}$ —velocity component	m/s	12-18
Re number	—	195-2694
We number	—	94-2204
Oh number	—	$6.3 \times 10^{-3}$ - $5.4 \times 10^{-2}$
Frequency	kHz	27.2-64.3
Test rig		
Material of the disc	—	Stainless steel
Size of disc	mm	150
$v_0$ —velocity component	m/s	9-30
Impact angle	—	4.1-65.4

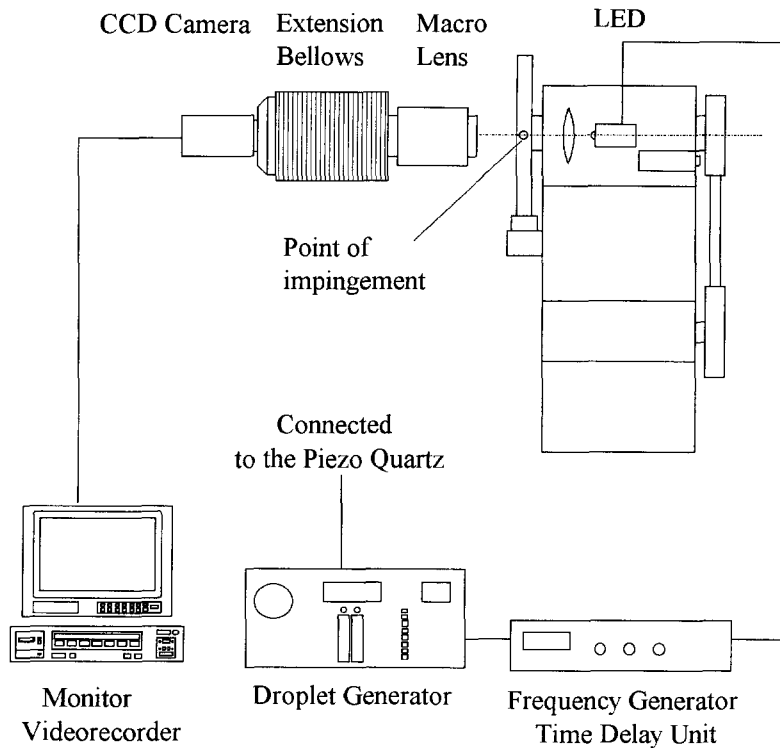


Figure 6. Schematic overview of the experimental instrumentation for visualization.

## 4. RESULTS

### 4.1. Visualization of the deformation process

The deformation, spreading and splashing of the droplets depend not only on the kinematic and fluid parameters of the primary droplets, but also on the ratio of the surface roughness compared to the droplet diameter. The non-dimensional surface roughness number  $S_r$  is 0.03 for disc 1 and 0.86 for disc 2, indicating that the surface roughness is negligible in the case of the smooth surface, whereas in the case of the rough surface a strong influence is expected. Therefore, the results for the smooth and rough surfaces are discussed in different sections.

#### 4.1.1. Smooth surface.

*High Reynolds numbers:* figure 7 shows a photograph of droplet splashing on disc 1, averaged over many individual events at the same phase. In figure 8 the derived schematical view of the splashing process is shown.

Table 2. PDA transmitting, receiving optics and measurement range

Transmitting and receiving optics		
Laserpower	mW	400
Wavelength		
Vertical component	nm	514.5
Horizontal component	nm	488.8
Focal length of the transmitting optics	mm	309.1
Focal length of the receiving optics	mm	310.8
Diameter of the measured volume	$\mu\text{m}$	240
Measurement range		
Focal length	mm	310.8
Droplets:		
Refractive index	—	1.306–1.367
Diameter range	$\mu\text{m}$	0–307
$w$ —velocity	m/s	–18.37–55.10
$v$ —velocity	m/s	–17.45–52.35

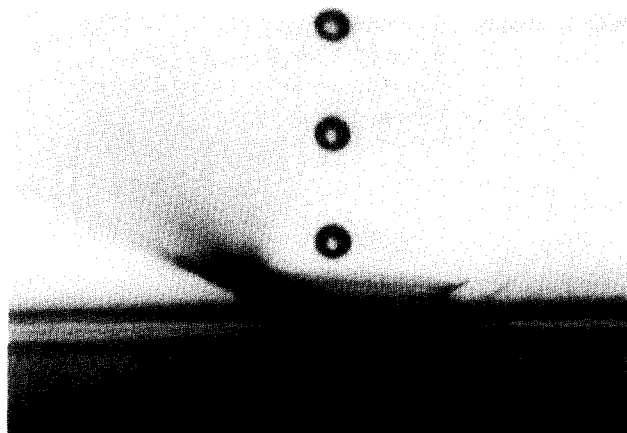


Figure 7. Splashing of a liquid droplet with  $Re = 598.8$ ,  $Oh = 0.0518$ ,  $K = 153.5$  and  $S_i = 0.03$  on a smooth surface, effective angle of impingement  $\alpha = 36^\circ$ .

As the droplet touches the surface, a liquid film spreads outwards. A corona around the deforming droplet is formed and grows in time as the droplet fluid continues to feed the film. Three coronas are visible on the frame, indicating that the time for the formation of the corona is much larger than the time for the deformation of the primary droplet. Hence the time evolution of the deformation process is recognizable in a single frame, demonstrating the high repeatability of the deformation process.

The deformation process can be summarized as follows. Once the lower half of the droplet has undergone deformation, the total volume flow rate into the wall film begins to decrease. Thus the corona, having been stretched in its radial expansion, also now has less fluid feeding the film and hence becomes thinner. An instability develops and leads to a circumferential wreath which propagates upward in the corona and finally results in a disintegration into secondary droplets.

*Low Reynolds numbers:* figure 9 shows a sequence of photographs describing the steps of the droplet deformation at a  $Re$  and  $Oh$  number of 215.4 and 0.0492, respectively. The corresponding schematic view of the deposition process with respect to time is presented in figure 10. At low  $Re$  numbers, the liquid film spreads around the point of impingement, but there is not enough momentum normal to the wall to form a corona. Rather, the kinetic energy necessary to overcome surface tension and gravity to form a corona is dissipated during the deformation process.

#### 4.1.2. Rough surface.

*High Reynolds numbers:* as pointed out by Weiss (1993), the nature of the surface target is an important factor in determining the outcome of a splashing event. To investigate this effect, disc 2 with a surface roughness approximately equal to the diameter of the primary droplets was used. Figure 11 shows the splashing of a droplet with  $Re = 589.9$  and  $Oh = 0.0518$ .

The deformation of the droplet upon impact is much more irregular than in the case of the smooth surface. The high tangential momentum of the incident droplet leads to a sudden and rigorous disintegration into secondary droplets. A corona and the associated instabilities before atomization are no longer identifiable. Furthermore, the concentration of the secondary droplets is much higher in front of the impingement point, as indicated by the dark area. A number of secondary droplets appear behind the impact location as a result of the surface roughness.

*Low Reynolds numbers:* The deposition of a droplet on a rough surface at low Reynolds number (figure 12) is similar to the deposition process for the technically smooth surface, in which the kinetic energy of the droplet is dissipated in the deformation process. Obviously the surface roughness in this range does not promote the splashing of the primary droplet.



Figure 8. Schematic view of the splashing process.

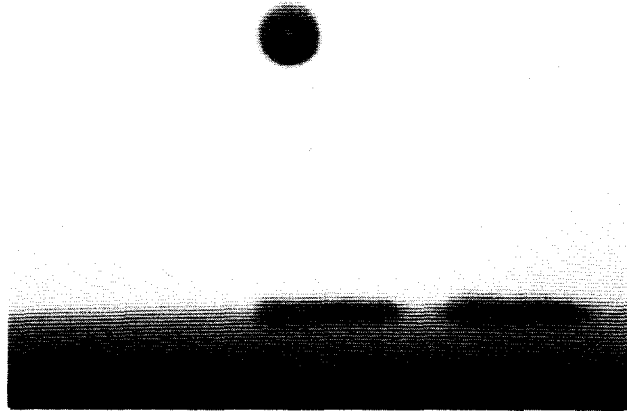


Figure 9. Deposition of a liquid droplet with  $Re = 251.4$ ,  $Oh = 0.0492$ ,  $K = 49.3$  and  $S_i = 0.03$  on a smooth surface, effective angle of impingement  $\alpha = 36^\circ$ .

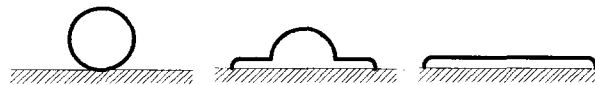


Figure 10. Schematic view of the deposition process.

#### 4.2. Correlation of the splashing and deposition event in terms of the $Oh$ and $Re$ number

The observed limits of deposition and splashing for both the smooth and the rough surface can be correlated in terms of the  $Re$  and  $Oh$  numbers. A remarkably strong correlation can be observed and is given by the relation  $K = Oh Re^{1.25}$ . A value of  $K$  exceeding 57.7 leads to incipient splashing, whereas  $K$  less than 57.7 leads to complete deposition of the liquid, as illustrated by the results presented in figure 13 (Mundo *et al.* 1993b).

The boundary line which separates deposition and splashing is parallel to the line that describes the decay of a liquid film from a nozzle, the so-called Ohnesorge line (Ohnesorge 1936). This indicates that the same physical process is responsible for the generation of the secondary spray. The strong correlation shown in figure 13 indicates that in the case of splashing, the influencing factor is the momentum of the primary droplets in the direction normal to the surface and not the total momentum vector.

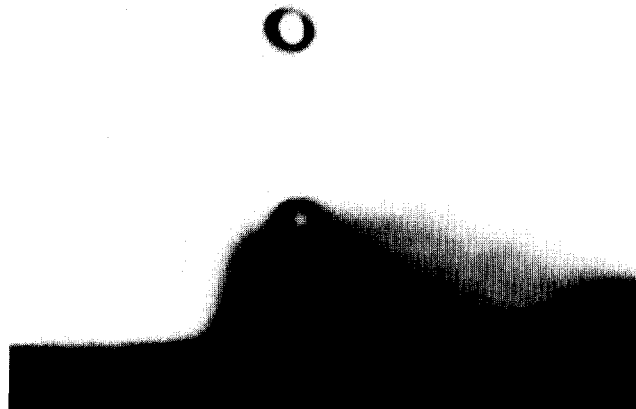


Figure 11. Splashing of a liquid droplet with  $Re = 598.8$ ,  $Oh = 0.0518$ ,  $K = 153.5$  and  $S_i = 0.86$  on a rough surface, effective angle of impingement  $\alpha = 36^\circ$ .

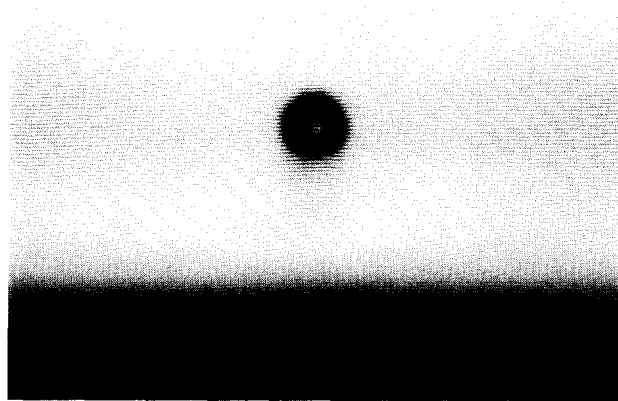


Figure 12. Deposition of a liquid droplet with  $Re = 251.4$ ,  $Oh = 0.0492$ ,  $K = 49.3$  and  $S_1 = 0.86$  on a rough surface, effective angle of impingement  $\alpha = 36^\circ$ .

4.3. Comparison with the theoretical approach

The correlation for incipient splashing obtained in figure 13 can be compared with the theoretical approach presented in section 2.2 [17]. However, to solve the equation the relation of the maximum diameter  $d_{max}$  to the diameter of the primary droplet  $d_0$  must be evaluated. From the measurements this was determined with  $\beta_{max} = d_{max}/d_0 \approx 2.3$  (Mundo *et al.* 1993a). The contact angle does not necessarily have to be the equilibrium angle, but it is considered to be fixed at  $\Theta \approx 75^\circ$ . In figure 14, [17] for these parameters is shown as “theoretical approach”. This relation matches the experimentally obtained correlation very well for  $Re$  numbers above 150. For  $Re$  numbers less than 150 the solution of [17] becomes irregular, indicating that for low  $Re$  numbers the assumption for the dissipative term in the momentum equation is not appropriate. Additionally the theoretical correlation deviates from the experimentally obtained correlation for  $Re > 2000$ .

4.4. Phase Doppler measurements

The secondary spray that occurs due to the splashing at sufficiently high  $K$  numbers was measured by means of a phase Doppler anemometer, described briefly in section 3.2.2. Figure 15

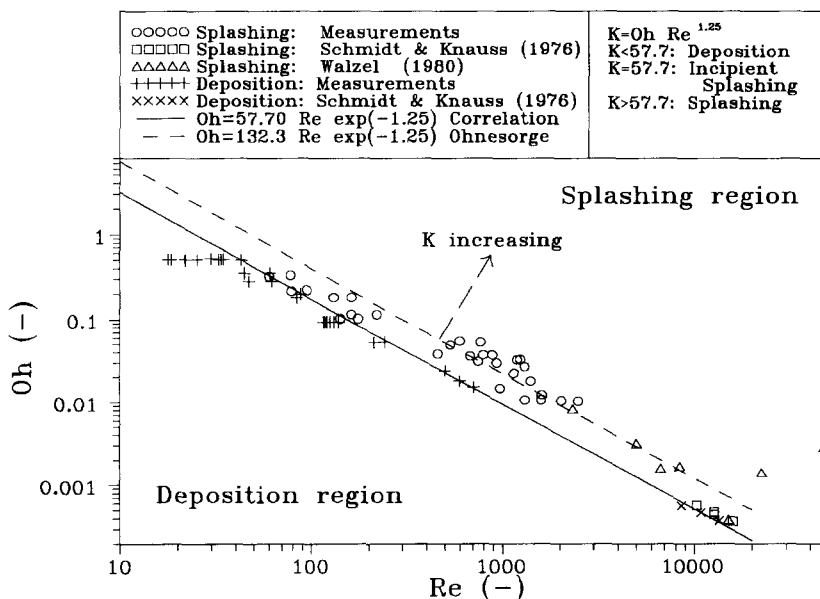


Figure 13. Limits for splashing and deposition of primary droplets.

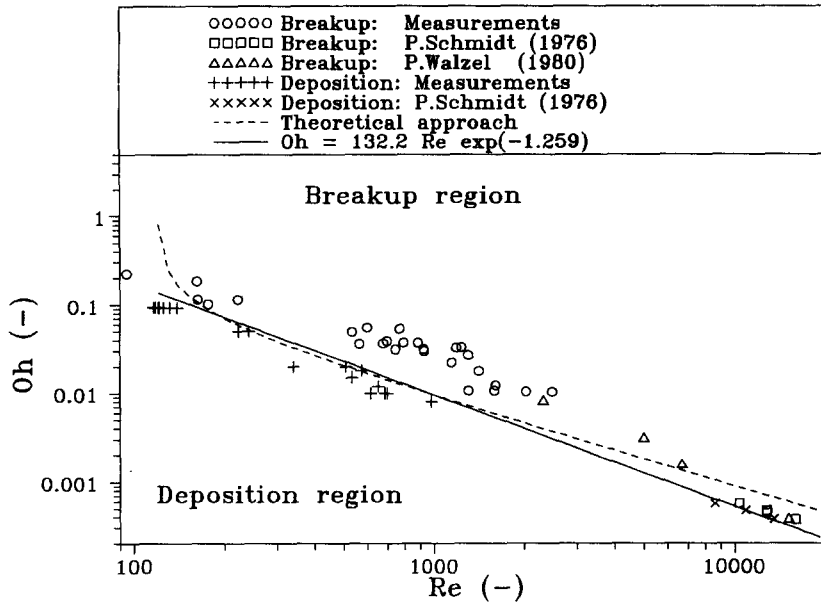


Figure 14. Empirical and theoretical correlations for incipient splashing.

indicates the matrix of measurement locations around the point of impingement in order to characterize the spatial distribution of the secondary spray. For obtaining a size distribution in front of and behind the point of impingement, the size distributions of the corresponding three measurement positions were averaged in their number distribution weighted with their rate of events.

In estimating the statistical reliability of the measured distributions first the statistical independence of individual droplet samples was investigated. This was done by computing the autocorrelation function [20] of the secondary droplet velocities and sizes over 50,000 samples. The measured autocorrelation functions, using the velocity or size of the secondary droplets is given in figure 16.

$$a(z) = \frac{(z(i) - \bar{z})(z(i + \Delta i) - \bar{z})}{\sigma_z^2} \quad [20]$$

Note that the autocorrelation was performed over the sequence of droplets as they arrived in the measurement volume, independent of their arrival time. This is in contrast with conventional autocorrelation functions, in which a time lag is used as an abscissa. The result reveals that for both

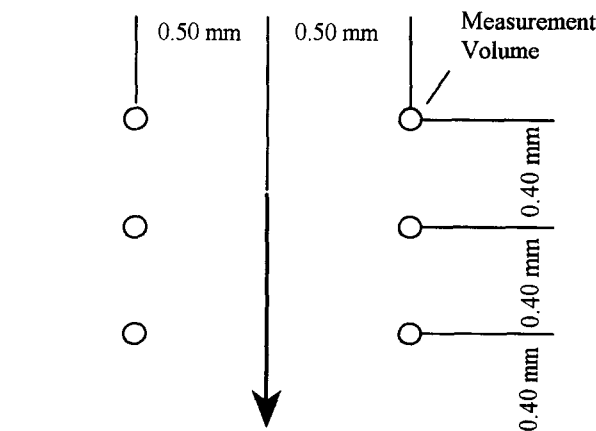


Figure 15. Measurement locations for the PDA measurements.

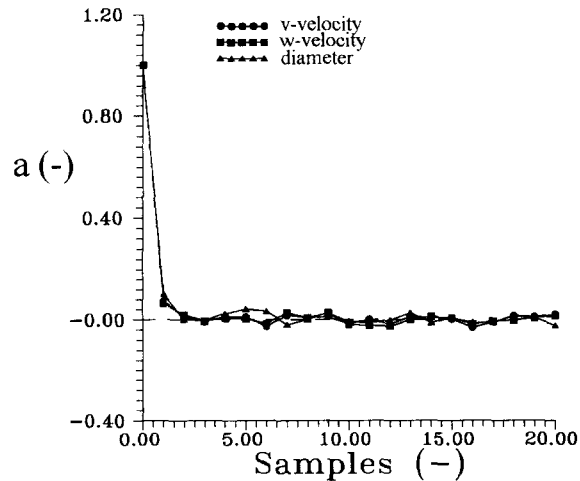


Figure 16. Autocorrelation function for the secondary spray.

velocity components each individual droplet is statistically independent since the autocorrelation function approaches zero at about two samples. For a statistically reliable distribution with a deviation of 1% therefore, a minimum number of samples must be measured as given by,

$$\epsilon^2 = \frac{1}{N} \left( \frac{\sigma_z^2}{\bar{z}^2} \right) \quad [21]$$

where  $\epsilon$  is the normalized standard deviation,  $\sigma_z^2$  is the standard deviation of the measured quantity,  $\bar{z}$  is the mean value of the process and  $N$  the number of samples.

Table 3 summarizes the results of this statistical analysis and the required minimum number of secondary droplet observations. In the present investigations a minimum number of 10,000 samples were measured.

#### 4.4.1. Diameter distributions.

*Smooth surface:* the size distributions corresponding to different values of the parameter  $K$  between 133 and 186 for three different liquids (i.e. ethanol, water, water–sucrose–ethanol) are summarized in figure 17. For completeness, [22] shows the parameters influencing the  $K$  value.

$$K = \sqrt{\text{We} \cdot \sqrt{\text{Re}}} = \text{Oh} \cdot \text{Re}^{1.25} = 4 \sqrt{\frac{\rho^3 d^3 u^5}{\sigma^2 \mu}} \quad [22]$$

The droplet size distribution has been normalized with the diameter of the primary droplets. The result indicates that the size distribution of the secondary droplets becomes narrower with increasing  $K$  value, associated with a decrease of the mean particle size. The distributions in figure 17 and the derived size statistics  $d_{10}$ ,  $d_{20}$ ,  $d_{30}$  and  $d_{32}$  are shown in figure 18. These indicate that especially the larger secondary droplets are absent at higher  $K$  values. A comparison of the size distributions obtained in front of the point of impingement with those behind the point of impingement reveals only minor differences, with the latter leading to slightly smaller mean size statistics.

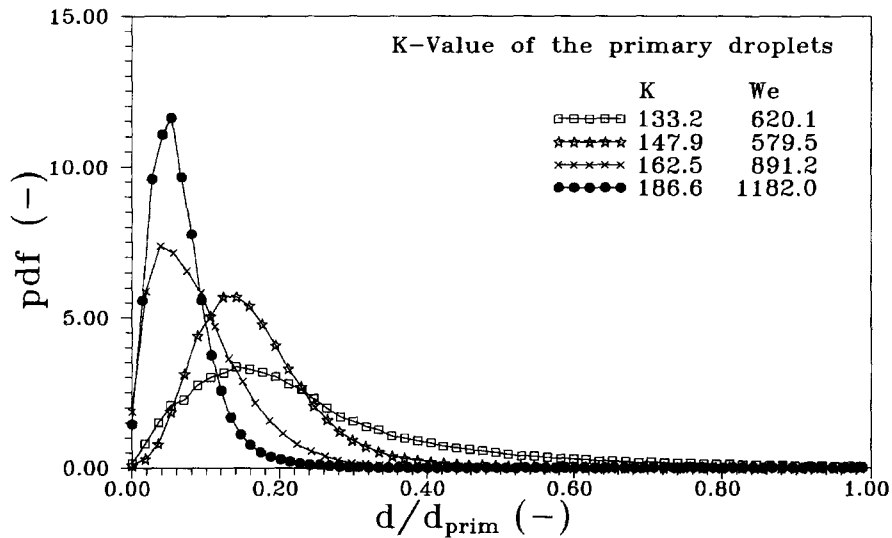
Table 3. Results of the statistical analysis

Number of samples over which an integral correlation exists	
$v$ -velocity component	1.106
$w$ -velocity component	1.124
Diameter	1.212
Minimum number of samples for $\epsilon = 1\%$	
$v$ -velocity component	6420
$w$ -velocity component	2652
Diameter	1782

Increasing the surface tension results in a smaller  $K$  value and therefore a narrower size distribution. Similar trends are observed for an increase in the viscosity of the liquid. In this respect the splashing phenomenon resembles the decay of a liquid sheet (Lefebvre 1989).

*Rough surface:* in figure 19 the size distributions of secondary droplets are shown for the rough surface (i.e. roughness factor  $S_t = 0.86$ ). The distributions show only minor differences for an increasing  $K$  value, both in front of and behind the impingement point. This indicates that the fluid properties and the kinematic parameters are not the most influential factors for the size distributions, but that the non-dimensional surface roughness number  $S_t$  determines the distributions. As described in section 4.1.2, a splash corona could not be observed for the rough surface. The disintegration of the droplet appears to be more immediate, indicating that the normal and tangential momentum of the primary droplet is almost directly transformed into surface energy in the case of a rough surface. The mean diameters shown in figure 20 vary only slightly with  $K$ .

a)



b)

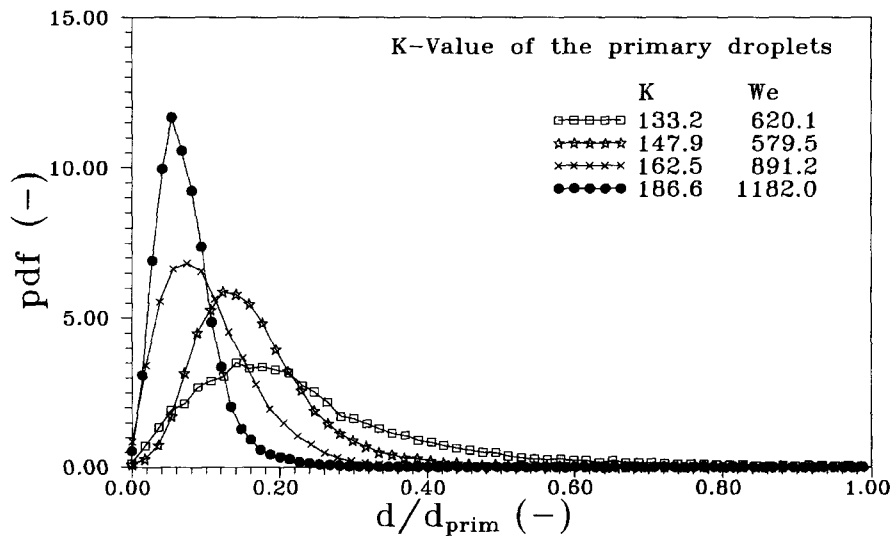


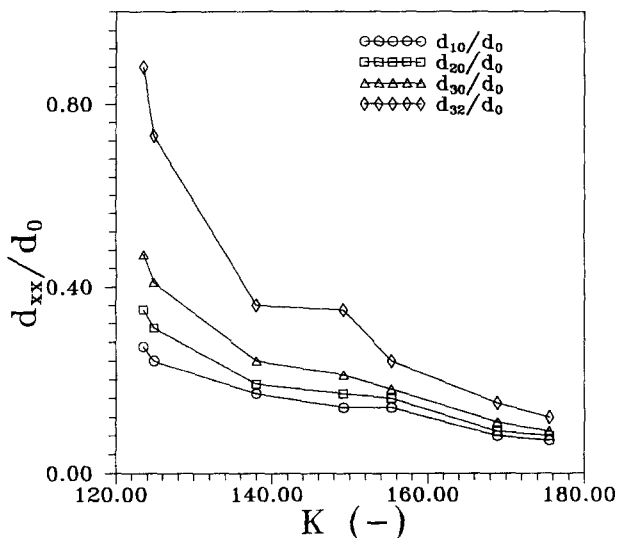
Figure 17. Secondary droplet diameter distribution for the smooth surface (a) in front of and (b) behind the point of impingement.

4.4.2. *Velocity distributions.* For formulating a statistical model of the droplet-wall impingement it is also necessary to determine the velocity of the secondary spray. Therefore, in this section the velocity distributions are investigated in a plane that includes the impingement and reflection velocity vector.

*Smooth surface:* figures 21 and 22 show the orientation and length of the velocity vectors for three size classes of the secondary droplets for a  $K$  number of 131. The orientation of the velocity vector of the secondary spray depends strongly on the incident angle of the primary droplet, therefore the outcome of two impact conditions (i.e.  $36^\circ$  and  $65^\circ$  impingement angle) are presented.

The most important result which can be obtained from figures 21 and 22 is that a small incident angle of the primary drop leads to a small reflection angle (i.e. both incident and reflection angle are measured with respect to the normal on the surface), and a large incident angle leads to a large reflection angle. The momentum of impingement is partially conserved and determines the flight

a)



b)

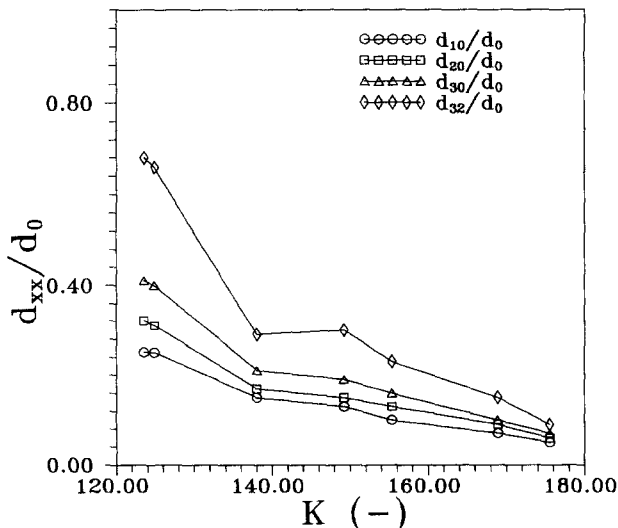


Figure 18. Characteristic mean diameters for the smooth surface (a) in front of and (b) behind the point of impingement.

direction of the secondary spray. On the other hand, the flight direction does not depend strongly on the size of the droplets, since the orientation of the velocity vectors are similar for the three size classes.

However, the dependency of the flight kinematics of the secondary spray on the impact conditions has to be analysed more closely. The reflection angle of the secondary droplets as a function of the impingement angle of the primary drop for a variation of the impact angle is summarized in figure 24. Each point represents an average of 30,000 samples. From a least square fit a linear correlation can be determined.

Moreover, the fluid properties, expressed by the  $K$  number as a function of the Ohnesorge and Reynolds numbers, are important influencing factors. The velocity distributions for three impact angles and various  $K$  values are summarized in figure 23 for the two velocity components. The velocity components are presented in non-dimensional form to obtain comparable results for

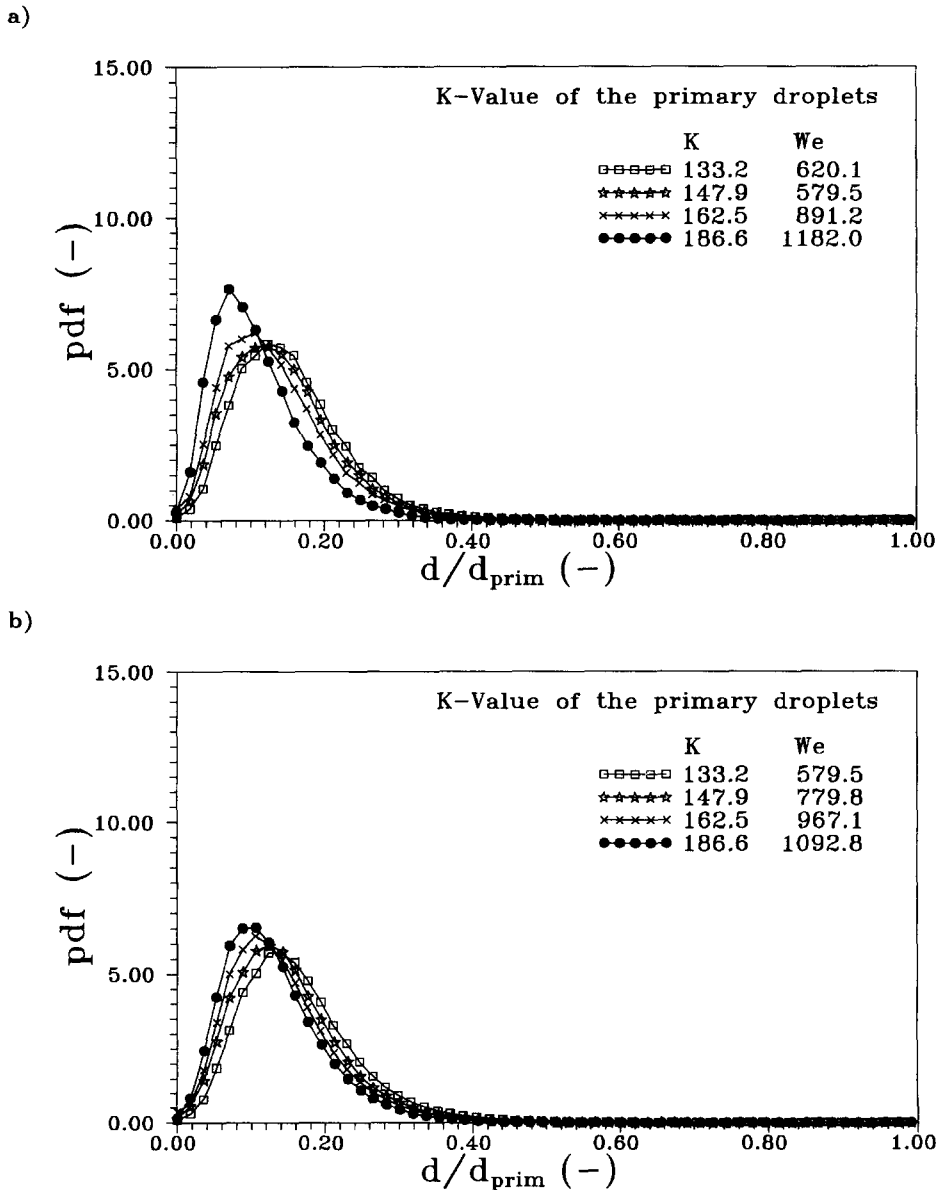
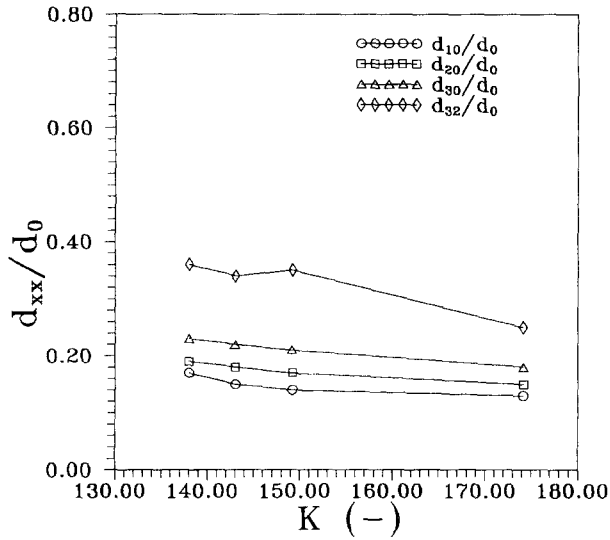


Figure 19. Secondary droplet diameter distribution for the rough surface (a) in front of and (b) behind the point of impingement.

a)



b)

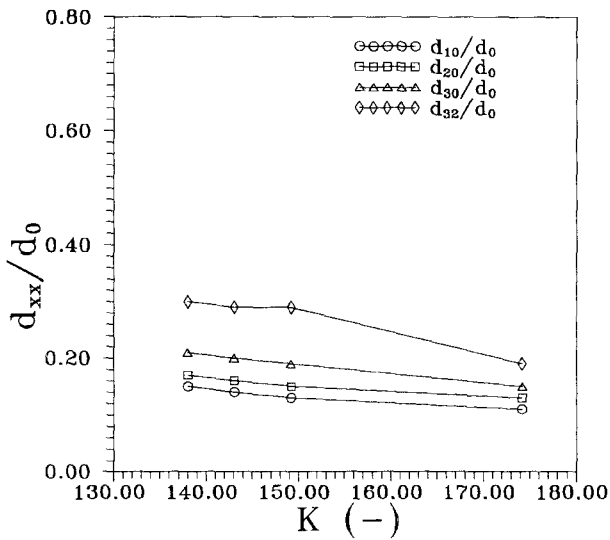


Figure 20. Characteristic mean diameter for the rough surface (a) in front of and (b) behind the point of impingement.

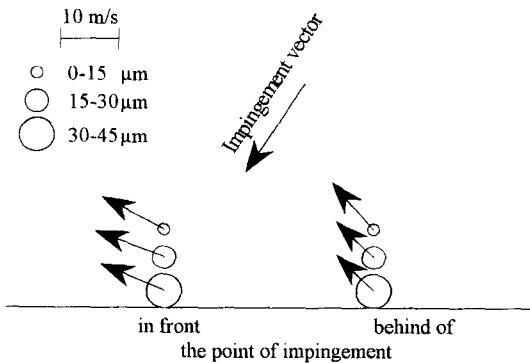


Figure 21. Velocity vectors for the impact on the smooth surface, impingement angle  $36^\circ$ , for three size classes of the secondary spray,  $K = 131$ .

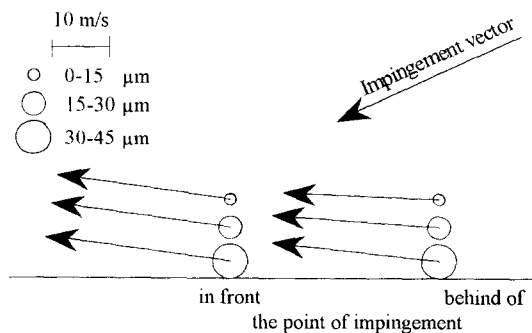


Figure 22. Velocity vectors for the impact on the smooth surface, impingement angle  $65^\circ$ , for three size classes of the secondary spray,  $K = 131$ .

different impingement velocities. Obviously the fluid properties (viscosity and surface tension) do not influence strongly the velocity and direction of secondary droplet motion, the distributions are nearly identical for the three  $K$  values. However, a large impingement angle and therefore a large ratio of tangential to normal momentum of the primary drop leads to a narrow distribution for

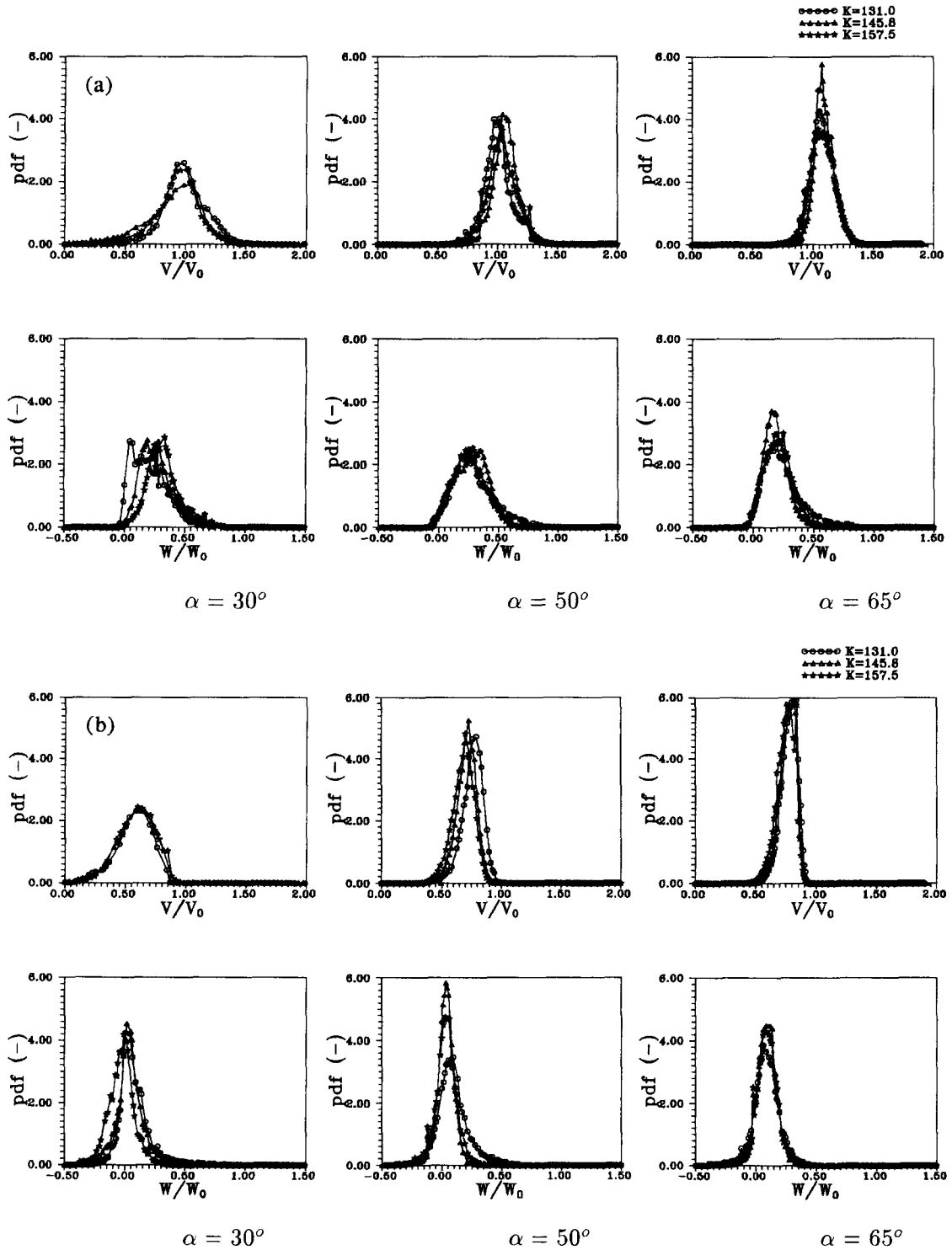


Figure 23. Velocity distribution for the smooth surface (a) in front of and (b) behind the point of impingement ( $S_i = 0.86$ ) for the secondary spray ( $v$  = tangential velocity component;  $w$  = normal velocity component).

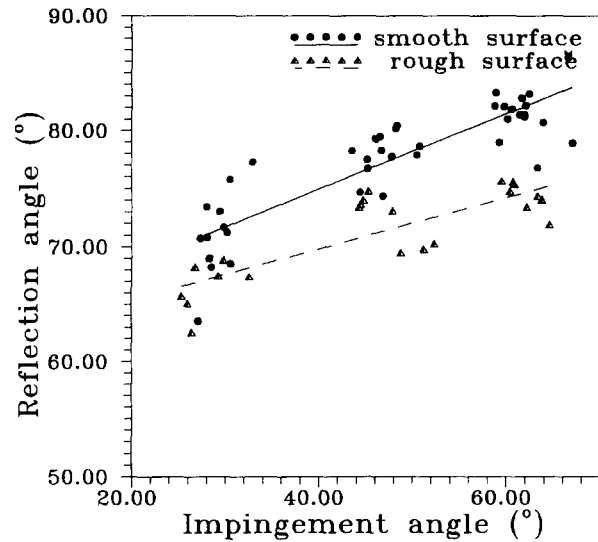


Figure 24. Dependency of the reflection angle on the impingement angle for the smooth and the rough surface (angles measured normal to the surface).

both measuring points (in front of and behind the point of impingement) and for both velocity components. It is surprising that in front of the impingement point the ratio of the tangential velocity of the secondary to the primary droplets is slightly larger than one, indicating that the momentum of the impinging drop in the normal direction is partially transformed into tangential momentum.

*Rough surface:* considering the velocity vectors for the secondary droplets obtained for the impingement on the rough surface, it is obvious that the roughness influences strongly the direction of the droplet motion (figures 25 and 26). In comparison to the velocity vectors presented in figures 21 and 22 for the impact on the smooth surface, the reflection angle with respect to the normal becomes smaller, because the tangential velocity component is reduced. This can be explained by the surface roughness which leads to a dissipation of the tangential momentum, and to a transformation of tangential momentum into normal momentum. A similar effect was observed for the interaction of a solid particle with rough walls (Sommerfeld *et al.* 1993). The reflection angle correlation with the impact angle of the primary droplet is given in figure 24. In fact, an almost linear relationship between the impingement angle and the reflection angle exists, but compared to the results obtained for a smooth surface the reflection angles are shifted to smaller values, especially for small impingement angles, indicating that the normal velocity component is

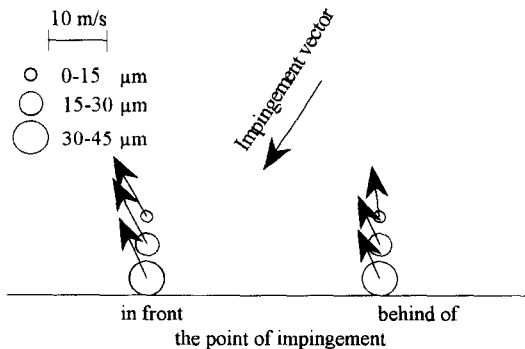


Figure 25. Velocity vectors for the impact on the rough surface, impingement angle  $36^\circ$ , for three size classes of the secondary spray,  $K = 131$ .

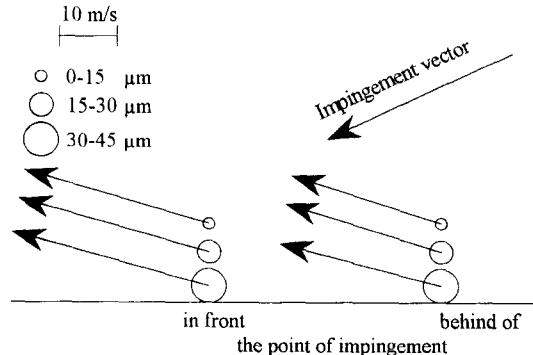


Figure 26. Velocity vectors for the impact on the rough surface, impingement angle  $65^\circ$ , for three size classes of the secondary spray,  $K = 131$ .

increased. This can be explained by the influence of the local surface roughness. The possibility of an impinging droplet hitting the “windward” side of the surface roughness element is greater than hitting the “leeward” side, leading to a transfer of tangential momentum into normal momentum (figure 28). Therefore, the mean normal velocity component of the splashed droplets

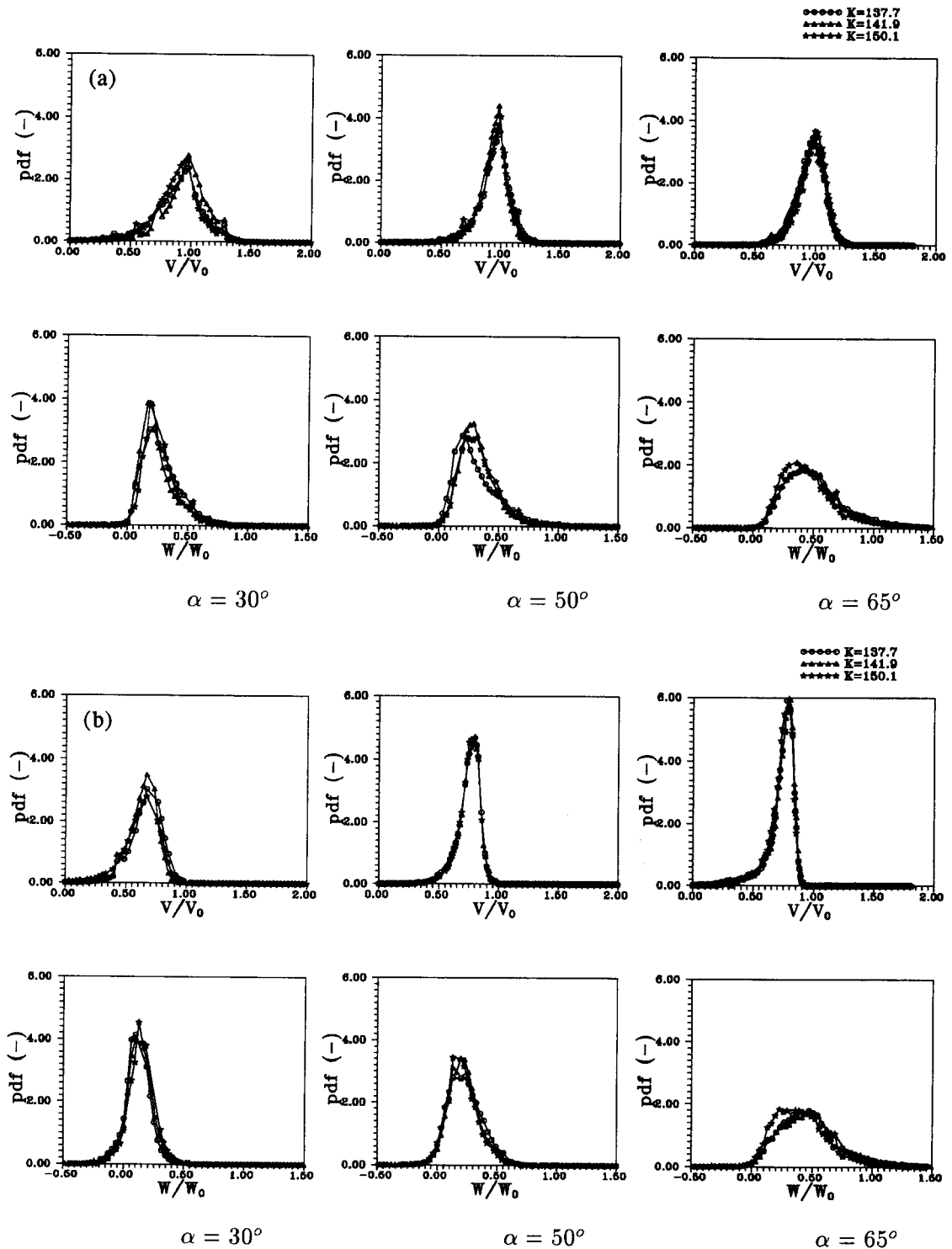


Figure 27. Velocity distribution for the rough surface (a) in front of and (b) behind the point of impingement ( $S_r = 0.86$ ) for the secondary spray ( $v$  = tangential velocity component;  $w$  = normal velocity component).

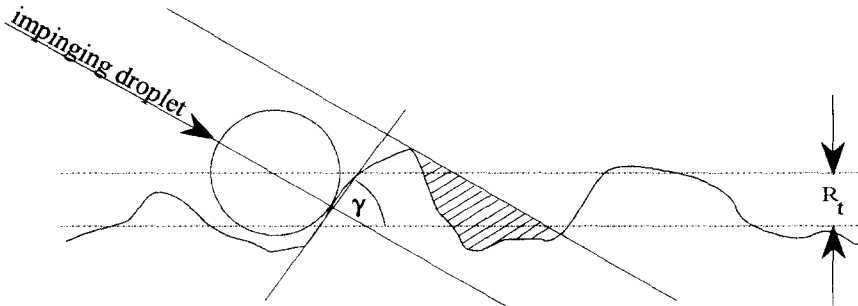


Figure 28. Influence of the surface roughness profile on the impingement process.

for an impact on the rough surface must be larger than the normal component for an impact on the smooth surface.

The influence of the fluid properties on the velocity probability density function are presented in figure 27. The distributions are very similar for the three  $K$  numbers, indicating that the flight direction does not depend on the fluid viscosity and surface tension in the case of a rough surface. An increase of the impingement angle of the primary drop leads to a narrower velocity distribution, and in front of the impingement point the ratio of the tangential velocities of the secondary droplets to the primary droplets is slightly larger than one, similar to the results obtained from the smooth surface. However, the ratio of the normal velocity component to the tangential is slightly larger than that obtained from the smooth surface.

## 5. CONCLUDING REMARKS

In this work the principal physical process of deformation and splashing of single droplets on surfaces was visualized and described. The fluid properties and the kinematic parameters were varied. It was shown that the splashing occurs due to the decay of the cylindrical sheet ('corona') which arises around the point of impingement for a smooth surface. The outcome of an impact—whether splashing or deposition occurred—depends on the  $Re$  and  $Oh$  numbers, which represent the fluid properties and kinematic impact parameters. For the case of splashing, the diameter and velocity distributions of the product droplets were measured around the point of impingement using a phase Doppler anemometer. The diameter distribution of the secondary droplets depends on the fluid properties (viscosity and surface tension) and kinematic parameters (velocity and size of the primary droplets) in the case of an impingement on a smooth surface.

Regarding the deformation and splashing when a liquid droplet impacts on a rough surface (roughness in the range of the diameter of the primary droplet), one finds that no splash-corona is formed and the diameter distribution of the secondary droplets becomes narrower with a smaller mean diameter. The distribution does not depend strongly on the fluid properties.

The velocity distributions show a remarkable strong dependence on the impingement kinematics. The tangential impact velocity is nearly completely transferred to the secondary droplets, for the impingement on the smooth and the rough surface. The normal momentum is only partially conserved, because the energy is dissipated during the impact and in the formation of the corona. For rough surfaces the splashing occurs under the influence of the local surface angle, leading to a transfer of tangential momentum into normal momentum. Therefore, the mean reflection angle to the normal of the secondary droplets decreases. For the derivation of a numerical droplet impact model it is necessary to measure the spatial mass flux around the point of impingement, which is the subject of further investigations.

*Acknowledgement*—The authors are grateful to the Deutsche Forschungsgemeinschaft (DFG), through grant TR194/7, for financial support of these investigations.

## REFERENCES

- ANDERS, K., ROTH, N. & FROHN, A. 1993 The velocity change of ethanol droplets during collision with a wall analysed by image processing. *Exp. Fluids* **15**, 91–96.

- BERGLUND, R. & LIU, B. B. 1973 Generation of monodispersed aerosol standards. *Envir. Sci. Technol.* **7**, 147–153.
- BOLLE, L. & MOUREAU, J. C. 1982 Spray cooling of hot surfaces. In *Multiphase Science and Technology*, Vol. 1. Hemisphere, Washington, DC.
- BRUNELLO, G., CALLERA, S., COGHE, A., COSSALI, G. E. & GAMMA, F. 1991 LDV and PDA analysis of spray-wall interaction. *ICLASS-91*, Gaithersburg, MD.
- CHANDRA, S. & AVEDIKIAN, C. T. 1991 On the collision of a droplet with a solid surface. *Proc. R. Soc. Lond. A* **432**, 13–41.
- COHEN, R. 1991 Shattering of a liquid drop due to impact. *Proc. R. Soc. Lond. A* **435**, 483–503.
- DANTEC, 1992 *Particle Dynamics Analyzer*. Skovlunde, Denmark.
- FADDEYEV, I. P., KHAVIYA, S. L. & MOSENZHNIK, B. Y. 1988 Oblique impingement of a spherical liquid droplet on a solid wall. *Fluid Mech.-Sov. Res.* **17**, No. 3.
- FOOTE, G. B. 1974 The water rebound problem: dynamics of collision. *J. Atm. Sci.* **32**, 390–402.
- VAN DER GELD, C. W. & SLUYTER, W. 1987 Numerical simulation of liquid drop collision with a rigid flat plate. *European Two-phase Flow Group Meeting*, Trondheim, Norway.
- HARDALUPAS, Y., OKAMOTO, S., TAYLOR, A. K. M. P. & WHITELAW, J. H. 1992 Application of a phase-Doppler anemometer to a spray impinging on a disc. *6th Int. Symp. on Appl. of Laser Technol. to Fluid Mech.*, Lisbon, Portugal.
- JAYARATNE, O. W. & MASON, B. J. 1964 The coalescence and bouncing of water drops at an air/water surface. *Proc. R. Soc. Lond. A* **280**, 545–565.
- LEFEBVRE, A. H. 1989 *Atomization and Sprays*. Hemisphere, New York.
- LEVIN, Z. & HOBBS, P. V. 1971 Splashing of drops on solid and wetted surfaces: hydrodynamics and charge separation. *Phil. R. Soc. Lond. A* **269**, 555–585.
- MUNDO, CH., SOMMERFELD, M. & TROPEA, C. 1993a Deposition von Flüssigkeitströpfchen an Wandoberflächen. LSTM Bericht 373/E/1993, Lehrstuhl für Strömungsmechanik, University of Erlangen-Nürnberg, Germany.
- MUNDO, CH., SOMMERFELD, M. & TROPEA, C. 1993b Experimental studies of the splashing and deposition of small liquid droplets impinging on a flat surface. *ICLASS 1994*, Prague, Czech Republic.
- NABER, J. D. & REITZ, R. D. 1989 Modelling engine spray/wall impingement. *Soc. Automot. Engng* 880107.
- NABER, J. D., ENRIGHT, B. & FARELL, P. 1988 Fuel impingement in a direct diesel engine. *Soc. Automot. Engng* 8801316.
- OHNESORGE, W. 1936 Die Bildung von Tropfen an Düsen und die Auflösung flüssiger Strahlen. *ZAMM* **16**, 355–358.
- ÖZDEMİZ, I. B. & WHITELAW, J. H. 1992 Impingement of an axisymmetric jet on unheated and heated flat plates. *J. Fluid. Mech.* **240**, 503–532.
- REIN, M. 1993 Phenomena of liquid drop impact on solid and liquid surfaces. *Fluid Dynam. Res.* **12**, 61–93.
- SCHMIDT, P. & KNAUSS, G. 1976 Prallzerstäubung von Flüssigkeiten bei Nichtbenetzung. *Chem. Ing. Tech.* **48**, 7.
- STOW, C. D. & HADFIELD, M. G. 1981 An experimental investigation of fluid flow resulting from the impact of a water drop with an unyielding dry surface. *Proc. R. Soc. Lond. A* **373**, 419–441.
- SOMMERFELD, M., HUBER, N. & WÄCHTER, P. 1993 Particle-wall collisions: experimental studies and numerical models. *ASME Fluids Engng Conf. 1993*, Washington, DC, U.S.A.
- WÄCHTERS, H. J. & WESTERLING, N. A. J. 1963 The heat transfer from a hot wall to impinging water drops in a spherical state. *Chem. Ing. Sci.* **21**, 1047–1056.
- WALZEL, P. 1980 Zerteilgrenze beim Tropfenprall. *Chem. Ing. Tech.* **52**, 338–339.
- WALZEL, P. 1990 Zerstäuben von Flüssigkeiten. *Chem. Ing. Tech.* **62**, 983–994.
- WATKINS, A. P. & WANG, D. M. 1990 A new model for diesel impaction on walls and comparison with experiments. *Chem. Engng Sci.* **21**, 1047–1056.
- WEISS, D. A. 1993 Periodischer Aufprall monodisperser Tropfen auf eine feste Wand. Ph.D. thesis, University of Göttingen.